COMMUNICATION

Check for updates

A phosphomolybdenum blue nano-photothermal agent with dual peak absorption and biodegradable properties based on ssDNA in near-infrared photothermal therapy for breast cancer†

Baoru Fang,[ab] Siqi Geng,[ab] Ke Wang,[ab] Fang Wang,[cb] Yiqing Zhou,[b] Jiaying Qin,[b] Shengnan Luo,[a] Yanping Chen[ab] and Zhangsen Yu ⦿ *[ab]

Photothermal therapy (PTT) stands as an emerging and promising treatment modality and is being developed for the treatment of breast cancer, prostate cancer, and a series of superficial tumors. This innovative approach harnesses photothermal agents (PTAs) that convert near-infrared light (NIR) energy into heat, efficiently heating and ablating localized lesion tissue. Notably, the low scattering of NIR-II (1000–1500 nm) band light within biological tissue ensures superior penetration depth, surpassing that of NIR I (700–900 nm) band light. Consequently, developing PTAs with excellent absorption performance and biocompatibility in the NIR-II band has attracted significant attention in photothermal therapy research. We successfully synthesized phosphomolybdenum blue (PMB) nanoparticles using single-strand DNA (ssDNA) as a template in this innovative study. Subsequently, we delved into this material's absorption characteristics and photothermal properties across the NIR-I and NIR-II spectral regions. Furthermore, we evaluated the therapeutic efficacy of PMB on 4T1 cells and tumor-bearing mouse models of breast cancer. Our findings revealed that PMB not only exhibits remarkable biocompatibility but also possesses stellar photothermal performance. Specifically, under 808 nm and 1064 nm laser irradiation, PMB achieved photothermal conversion efficiencies of 21.37% and 28.84%, respectively. Notably, compared to 808 nm laser irradiation, even when transmitting through a 2 mm thick tumor tissue homogenate, the 1064 nm laser irradiation maintained a robust tumor ablation effect. What's more, PMB possesses critical pH-responsive degradation properties. For instance, PMB nanoparticles degrade rapidly under physiological conditions (pH 7.2–7.4) while degrading slower in the acidic tumor microenvironment (pH 6.0–6.9). This unique characteristic significantly mitigates the systemic toxicity of PMB and enhances the safety of photothermal therapy implementation. Moreover, our study represents the first instance of utilizing ssDNA

New concepts

This study demonstrates a novel method for synthesizing photothermal nanomaterials (PTAs). ssDNA and ammonium molybdate are synthesized using a simple and convenient one-pot hydrothermal method. The PTAs (i) synthesize by using ssDNA as a template; (ii) degrade slowly in the acidic tumor microenvironment (pH 6.0–6.9) but rapidly degrade under physiological conditions (pH 7.2–7.4) so that normal tissues around the tumor are protected from burns; (iii) have absorption in both the NIR-I and NIR-II regions, and can achieve deeper photothermal therapy in the NIR-II region. The results show that the PTAs have good photothermal conversion efficiency and can effectively ablate tumors. Our work provides effective and safe PTAs, and leads to a deeper understanding of photothermal therapy for deep tumors to realize tumor therapy more effectively.

as a template for synthesizing a PMB nano photothermal agent and demonstrating its exceptional tumor thermal ablation efficacy. This groundbreaking work offers novel insights into the development of safe, efficient, and pH-responsive photothermal agents for cancer therapy.

Introduction

Photothermal therapy (PTT) is an innovative cancer treatment modality renowned for its efficiency, safety, and ease of operation.[1,2] This technique relies on photothermal agents (PTAs) that transform near-infrared (NIR) light energy into heat, effectively heating up and ablating tumor tissue.[3,4] The efficacy of PTT is primarily influenced by the excitation light and PTA.[5] The commonly used excitation light in PTT is the first NIR window (NIR-I; 700–900 nm) and the second NIR window (NIR-II; 1000–1500 nm). While NIR-I laser-based PTT

[a] School of Life and Environmental Sciences, Shaoxing University, Shaoxing City, Zhejiang Province, 312000, P. R. China. E-mail: yzs@usx.edu.cn

[b] Laboratory of Nanomedicine, Medical Science Research Center, School of Medicine, Shaoxing University, Shaoxing City, Zhejiang Province, 312000, P. R. China

[c] The First Clinical Medical College, Wenzhou Medical University, Wenzhou, Zhejiang Province, 325000, P. R. China

† Electronic supplementary information (ESI) available. See DOI: https://doi.org/10.1039/d4nh00464g
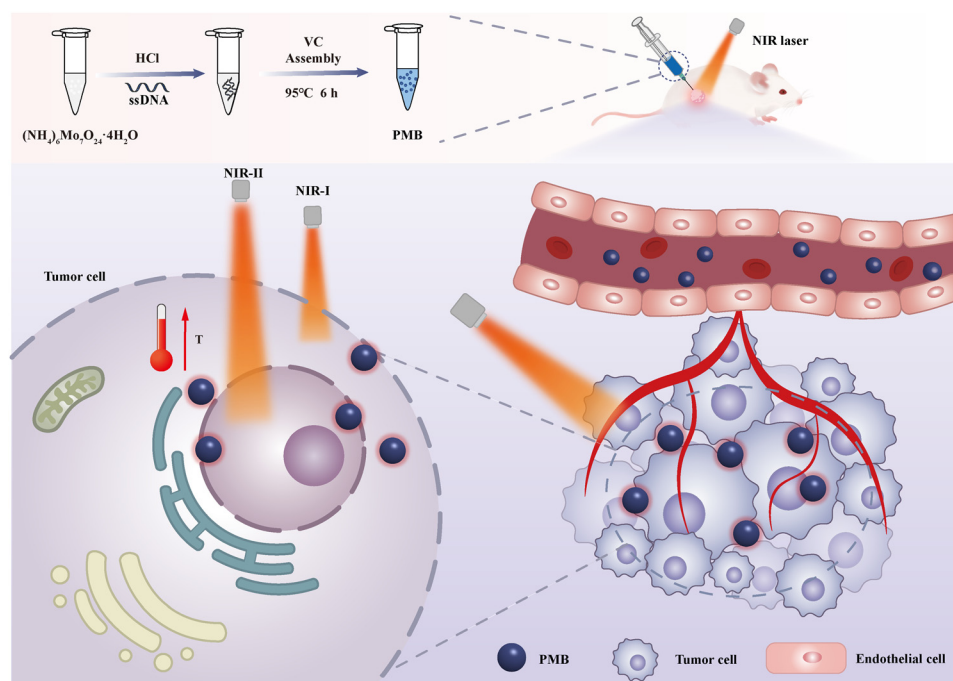
has been extensively studied, its limited penetration depth in biological tissues often poses a challenge for effectively treating deep tissues or large-volume solid tumors.

Consequently, current PTT methods are primarily suited for superficial tumors,[1,6] such as melanoma and adenocarcinoma. In contrast, the NIR-II band laser offers distinct advantages. Due to its lower scattering coefficient in biological tissues, it achieves deeper penetration, making it a more promising candidate for PTT in deep tumor tissues.[7] The urgent need to implement PTT for deep tumors has prompted many researchers to study the potential application value of NIR-II region lasers in PTT.[8–13] Therefore, developing ideal PTAs that exhibit high photothermal conversion efficiency within the biological tissue's optical window in the NIR-II region is crucial for the successful clinical translation and application of PTT for deep tumor tissues.

PTA is pivotal in achieving effective PTT for deep tumors.[14] The ideal PTA should possess four key attributes: (1) exceptional light absorption in the NIR-II region, (2) high photothermal conversion efficiency, (3) "smart" responsiveness to the tumor microenvironment, and (4) excellent biocompatibility.[8] Currently, a diverse range of photothermal nanomaterials have been developed for PTT, encompassing nanogold and other precious metal nanoparticles,[15–17] carbon nanomaterials,[18] metal oxides,[19] quantum dots,[20] and semiconductor nanomaterials.[21] Semiconductor nanomaterials, in particular, stand out as PTA with remarkable performance due to their unique properties, such as localized surface plasmon resonance (LSPR), stability, and ease of modification. Molybdenum-based nanomaterials stand out as essential semiconductor nanomaterials that have garnered significant

attention in recent years for their potential in PTT, making them a research hotspot in the biomedical field. MoO_{3-x}, also known as "molybdenum blue". Recent reports suggest that the transition between Mo^{+5} and Mo^{+6} in the valence charge transfer transition induces a pronounced LSPR in blue MoO_{3-x} nanosheets.[22–25] These MoO_{3-x} nanomaterials have been effectively utilized for NIR-mediated cancer PTT/PDT.[24] Furthermore, they are pH-sensitive and possess pH-responsive near-infrared absorption properties.[25] Despite the significant advantages of MoO_{3-x} nanomaterials in cancer photothermal treatment, there are still challenges to be addressed in practical applications, such as enhancing the biocompatibility of molybdenum-based nanomaterials.[26–28] These challenges require further in-depth research on solutions to fully utilize MoO_{3-x} nanomaterials for NIR-II region PTT, providing novel nanophotothermal therapeutic agents for thermal ablation of deep tumor tissues.

DNA is a natural biological macromolecule with remarkable biocompatibility and precise assembly controllability, making it a compelling candidate for nanotechnology applications. DNA nanotechnology exhibits immense potential in cancer treatment and has gained significant attention.[29] DNA nanomaterials, such as DNA origami or DNA nanoflowers, can undergo acceptable structural customization and excellent biocompatibility.[30,31] These materials hold tremendous promise for delivering therapeutic nucleic acids or small molecular drugs into cells for diverse therapeutic applications. However, there are still challenges in the preparation process of DNA nanomaterials. The synthesis process is often intricate, requiring complicated sequence design and strict control.[32,33] Therefore, simplifying the complex synthesis process of DNA

Scheme 1 The scheme of self-assembly PMB for cancer therapy.

nanomaterials remains a pivotal challenge in this field. In recent years, few reports have been on synthesizing DNA–metal nanomaterials, which utilize DNA as a template *via* a straightforward and convenient one-pot hydrothermal approach.

In this work, using single-stranded DNA (ssDNA) as a template and Vitamin C (VC) as a reducing agent, under acidic reaction conditions, PMB nanoparticles were synthesized based on the interaction between ammonium molybdate and ssDNA phosphate ions using a simple one-pot hydrothermal method. PMB possesses exceptional light absorption properties, high NIR-I/II region photothermal conversion efficiency, and pH-responsive degradation characteristics (Scheme 1), attributes significantly enhancing PMB's biosafety. It is worth noting that PMB nanoparticles exhibit significant PTT therapeutic effects on superficial tumor tissues in both NIR-I and NIR-II regions, and in deep tumor PTT, the implementation of NIR-II region PTT still has excellent therapeutic efficacy. In addition, *in vitro* drug blood compatibility and *in vivo* acute toxicity experiments indicated that PMB has low toxic side effects and good biocompatibility. Therefore, PMB is a safe and effective nano photothermal agent with good clinical application prospects.

Results and discussion

Morphological characterization of PMB

To elucidate the formation mechanism of PMB, we systematically studied the impact of various synthetic parameters on the generation of nanoparticles. These parameters include reaction time, ssDNA concentration, VC concentration, reaction temperature, and pH (Table 1). The TEM images (Fig. S1, ESI†) revealed that an increase in ssDNA concentration led to a decrease in the particle size of PMB. This decrease is primarily attributed to the rise in ssDNA templates, which produce more

PMB nanoparticles within the reaction system. Additionally, the ssDNA concentration did not significantly affect the morphology and size of PMB. However, we observed a gradual reduction in the particle size of PMB as the reaction time increased. Specifically, when the reaction time was set at 3 h, 6 h, 12 h, and 24 h, the average particle size of PMB was 50.36 ± 5.48 nm, 33.1 ± 3.36 nm, 37.38 ± 4.17 nm, and 11.01 ± 2.31 nm, respectively. After 24 hours of reaction, the particle size of PMB further decreased and exhibited adhesion, likely due to the degradation of ssDNA caused by an overly extended reaction time. Furthermore, we found that the reaction temperature and HCl concentration significantly impacted the PMB. At different reaction temperatures and HCl concentrations, the morphology and particle size of the resulting PMB varied significantly, though the specific influence mechanism remains to be determined. The zeta potential measurements (Fig. S2 and S3, ESI†) indicated that PMB synthesized under varying reaction conditions exhibits a consistently negative charge, with Zeta potentials below -30 mV, which suggests that the PMB dispersions synthesized under these conditions are relatively stable.

The ultraviolet-visible-near-infrared absorption spectra (Fig. S4, ESI†) revealed that the molar concentration of ssDNA and the concentration of VC had minimal influence on the absorption spectra of PMB. However, as the HCl concentration increased, the absorption of PMB in the NIR-II region gradually decreased. In contrast, with increasing synthesis time, the absorption of PMB in the NIR-II region first increased and then decreased, reaching a maximum when the synthesis time was 6 hours. Moreover, as the synthesis temperature increased, the absorption of PMB in NIR-II gradually weakened. Therefore, the synthesis temperature significantly impacted the PMB's absorption ratio ($A_{1064\text{ nm}}/A_{808\text{ nm}}$). Careful consideration of the impact of the above reaction conditions on PMB, this work successfully synthesized PMB using the optimal conditions of 25 μM ssDNA, 10% VC, 2% ammonium molybdate, and 1.2 mol L^{-1} HCl in a 95 °C water bath for 6 hours. TEM images revealed that PMB exhibited a spherical shape, with an average particle size of 33.1 ± 3.6 nm (Fig. 1(a)) and a uniform particle size distribution.

Further analysis of the hydration kinetics radius of PMB indicated a narrow particle size distribution, with an average size of 255 ± 37.5 nm (Fig. 1(b)). This discrepancy between TEM and DLS measurement results can be attributed to the flexibility of ssDNA, which serves as a template for PMB and is easy to extend in solution, resulting in a larger apparent size in DLS. The zeta potential of PMB was determined to be -44.1 ± 3.81 mV (Fig. 1(c)), indicating the excellent stability of the PMB dispersion. High-resolution transmission electron microscopy (HRTEM) coupled with element distribution mapping revealed that PMB comprises Mo, P, O, and N elements. Specifically, P and N originate from ssDNA, while Mo stems from ammonium molybdate, confirming the formation of PMB through the reaction between ssDNA and ammonium molybdate (Fig. 1(d) and (e)). Fourier transform infrared spectroscopy (FTIR) analysis shows the characteristic absorption peaks of various

Table 1 Different experimental conditions for synthesizing PMB nanoparticles

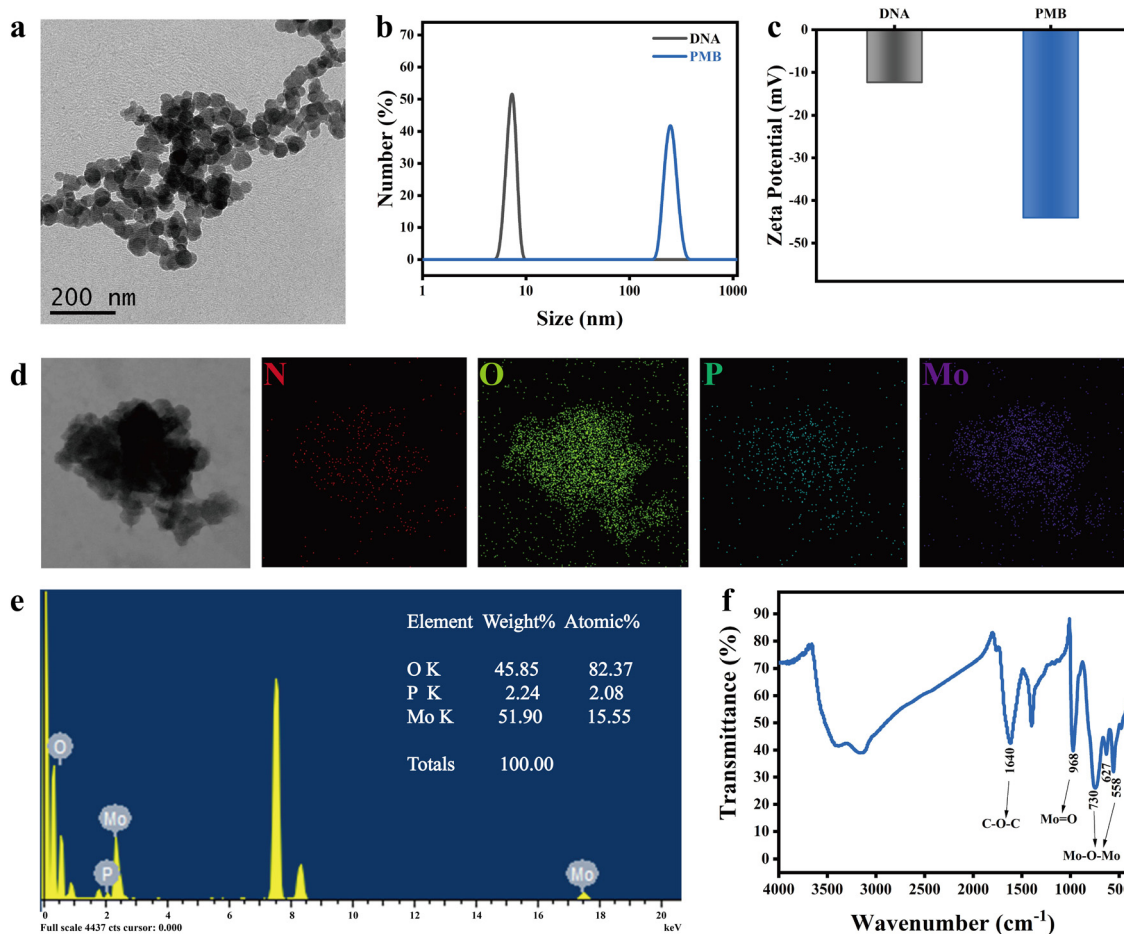| Group	Influencing factors	ssDNA (μM)	VC (%)	Time (h)	Temperature (°C)	HCl (mol L^{-1})
a	Effect of ssDNA	**25**	10	6	95	1.2
b		**50**	10	6	95	1.2
c		**75**	10	6	95	1.2
d		**100**	10	6	95	1.2
e	Effect of VC	25	**5**	6	95	1.2
f		25	**10**	6	95	1.2
g		25	**15**	6	95	1.2
h		25	**20**	6	95	1.2
i	Effect of time	25	10	**3**	95	1.2
j		25	10	**6**	95	1.2
k		25	10	**12**	95	1.2
l		25	10	**24**	95	1.2
m	Effect of temperature	25	10	6	**25**	1.2
n		25	10	6	**37**	1.2
o		25	10	6	**60**	1.2
p		25	10	6	**95**	1.2
q	Effect of HCl	25	10	6	95	**0.6**
r		25	10	6	95	**1.2**
s		25	10	6	95	**1.8**
t		25	10	6	95	**2.4**

Fig. 1 PMB morphology and performance characterization (a) TEM image of PMB; (b) and (c) DLS distribution and zeta of PMB and DNA; (d) the corresponding essential elemental mapping of PMB; (e) the corresponding essential elemental of PMB; (f) FTIR spectrum of PMB.

functional groups in the synthesized PMB (Fig. 1(f)). The absorption peaks at 558 cm^{-1}, 627 cm^{-1}, and 730 cm^{-1} correspond to the Mo–O–Mo stretching vibration. At the same time, 968 cm^{-1} represents the Mo=O stretching vibration. Additionally, the peak at 1640 cm^{-1} is attributed to the stretching vibration of the C–O–C group. These findings demonstrate the successful synthesis of PMB nanoparticles using ssDNA as a template. Moreover, there are no pronounced diffraction peaks on the XRD diffraction pattern of PMB nanoparticles, indicating that PMB nanoparticles have an amorphous structure (Fig. S5, ESI†).

pH-responsive degradation of PMB

Mo ion has different valence states under various pH conditions [24]. Under acidic conditions, Mo is a blue Mo^{+5} species, while under alkaline conditions, Mo is oxidized to a colorless Mo^{+6} species. As shown in Fig. 2(b), PMB degrades rapidly under weakly alkaline and physiological conditions (such as pH = 7.4 and pH =7.0 saline), with a degradation rate of 81.5% and 70.6% within 1 h, respectively, while it is relatively stable under acidic conditions (pH = 6.0), with a degradation rate of only 25.8% within 1 h. After 1 h, the degradation of PMB

gradually stabilized under acidic and alkaline conditions. Because PMB is oxidized to colorless PMB (Mo^{+6}) under alkaline conditions, its absorption in the near-infrared region is significantly reduced, and the photothermal effect is weakened. After mixing PMB nanoparticles with Saline with pH = 7.4 and pH = 7.0 for 0, 1,2 h, the temperature rise of PMB nanoparticle dispersion very nearly the same, respectively, after being irradiated by 808 nm laser (1.5 W, 5 min). The temperature rise effect of PMB dispersion after mixing for 1 h is close to that of pure water under the same conditions. However, after mixing PMB with Saline with pH = 6.0 for the same time, the temperature rise was 11.9 °C, 10.4 °C, and 8.4 °C, respectively (Fig. 2(c) and Fig. S6, ESI†), significantly higher than that of Saline with pH = 7.4. PMB has been proven to have excellent pH responsiveness and can maintain photothermal performance under acidic conditions, but it does not possess photothermal properties due to degradation under alkaline conditions.

Photothermal performance analysis of PMB *in vitro*

The UV-vis-NIR absorption spectra of PMB demonstrate its exceptional absorption capabilities in the near-infrared region, spanning the biological tissue optical windows of NIR-I and
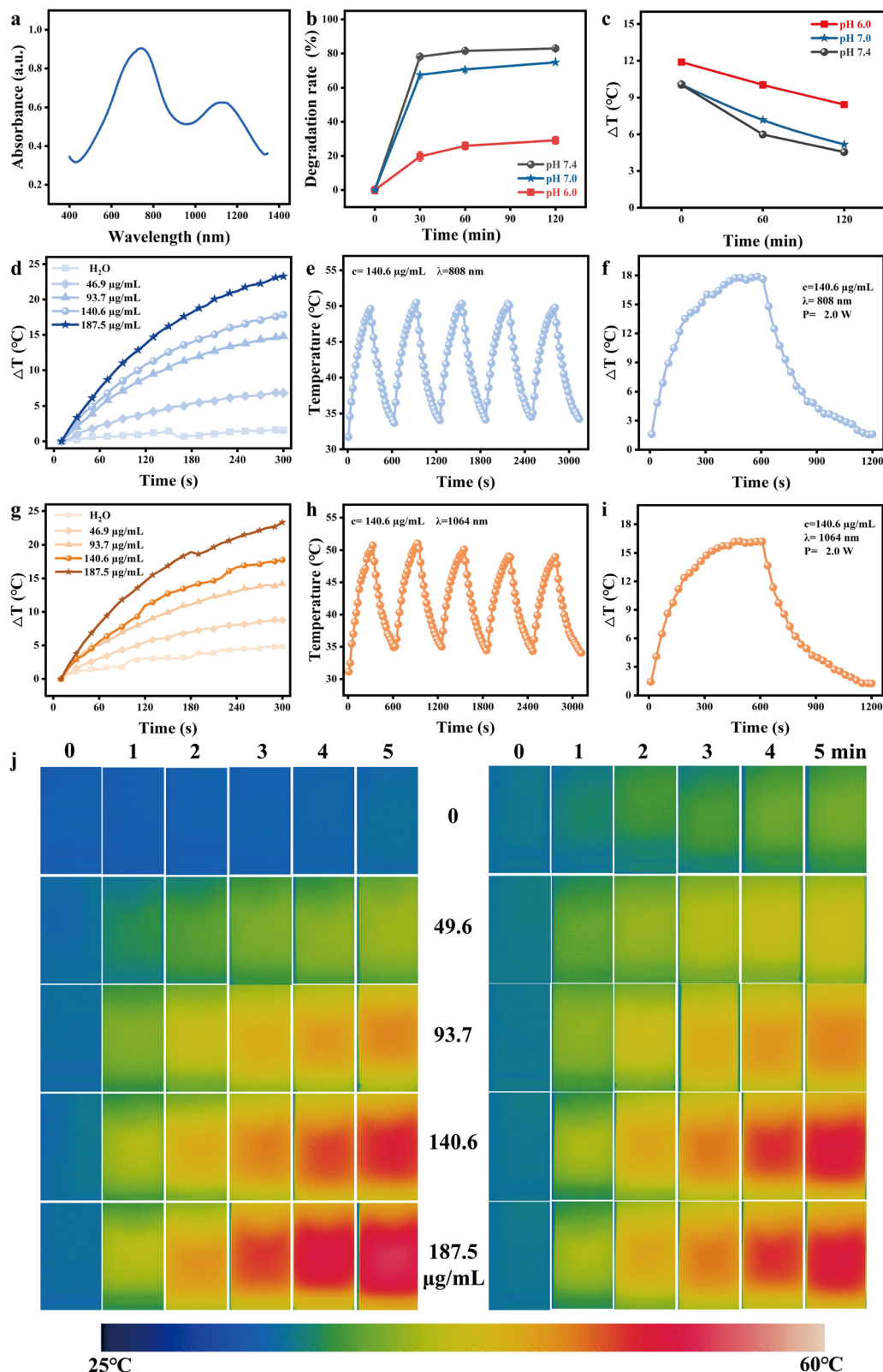
Fig. 2 Photothermal performance of PMB. (a) UV-vis absorption spectrum of PMB. (b) The degradation rate of PMB (140.6 μg mL^{-1} 1 mL) in different pH (6.0, 7.0, 7.4) Saline and (c) temperature rise curves after degradation (808 nm 1.5 W, 5 min). Photothermal heating curves of PMB aqueous suspensions (1 mL) with different concentrations under the irradiation of (d) 808 nm (g) 1064 nm lasers. Photothermal stability of PMB aqueous suspensions (1 mL) under (e) 808 nm and (h) 1064 nm lasers through repeated heating and cooling measurements. Heating of PMB aqueous suspensions (1 mL) with (f) 808 nm and (i) 1064 nm laser irradiation for 10 min and then cooling at ambient environment; (j) thermal imaging of PMB under (left) 808 nm and (right) 1064 nm laser irradiation.

Table 2 The relevant experimental data and calculation results used to calculate the photothermal conversion efficiency under 808 nm and 1064 nm laser irradiation

	τ	h_s	$T_{max} - T_{sur}$	Q_{dis}	$-A_{808/1064\,nm}$	$10^{-A_{808/1064\,nm}}$	η
H_2O	1043.76	0.0040	0.81	0.0023			
PMB under 808 nm laser	420.22	0.0099	24.89		−0.636	0.2312	21.38
PMB under 1064 nm laser	389.55	0.0107	26.96		−0.477	0.3334	28.84

NIR-II, with absorption peaks at 740 nm and 1085 nm, respectively (Fig. 2(a)). To evaluate the photothermal properties of PMB dispersions in these biological tissue windows, we irradiated them with 808 nm and 1064 nm lasers. Notably, the photothermal temperature rise of PMB dispersion exhibited an intense concentration-dependent behavior (Fig. 2(d) and (g)). Upon irradiation with 808 nm and 1064 nm lasers, the temperature of PMB dispersion rose rapidly within 5 minutes. For instance, at a concentration of 187.5 μg mL^{-1}, both lasers induced a temperature increase of approximately 23.3 °C in 5 minutes. Under identical conditions, pure water experienced a temperature rise of less than 5 °C, while PMB's temperature increase was sufficient to achieve tumor cell ablation. Thermal images captured by the thermal imager revealed temperature changes in PMB dispersions of varying concentrations aligned with the temperature rise curve (Fig. 2(j)). Furthermore, the increasing temperature of PMB dispersions positively correlates with the laser power density of NIR (Fig. S7, ESI†). After five heating/cooling cycles (Fig. 2(e) and (h)), the maximum temperature rise of PMB dispersion remained stable, indicating excellent photothermal stability. PMB's photothermal conversion efficiency (η) was calculated using the rise and fall curve under 808 nm and 1064 nm laser irradiation. Following a 10-minute laser exposure, the temperature of PMB rose by

17.85 °C and 16.38 °C, respectively. Calculations reveal that the photothermal conversion efficiency of PMB stands at 21.4% under 808 nm laser irradiation and 28.8% under 1064 nm (Fig. 2(f), (i), Fig. S8, ESI† and Table 2). The findings indicate that PMB possesses remarkable photothermal properties, making it an ideal candidate for use as a photothermal agent in the NIR I/II region for tumor photothermal therapy.

Study on photothermal effect of deep tissue *in vitro*

The photothermal efficacy of 808 nm and 1064 nm lasers in treating deep tumor tissue was assessed by analyzing their treatment effect through varying thicknesses of tumor tissue homogenates, as illustrated in Fig. 3(a). These two lasers' biological tissue penetration capabilities were compared (Fig. 3(b) and (c)). The laser power meter captured the residual laser power of 808 nm and 1064 nm lasers after traversing tumor homogenates of differing thicknesses (0, 2, 4, 6, 8, and 10 mm). Notably, at the same power level, the 1064 nm laser demonstrated a higher penetrating power through tumor homogenates at all depths than the 808 nm laser. The most significant disparity was observed at a tissue depth of 1 mm, where the 1064 nm laser's power was 1.47 times greater than that of the 808 nm laser (Fig. 3(d)). Precisely, when the initial laser power was set at 3.0 W, the residual power of the 1064 nm
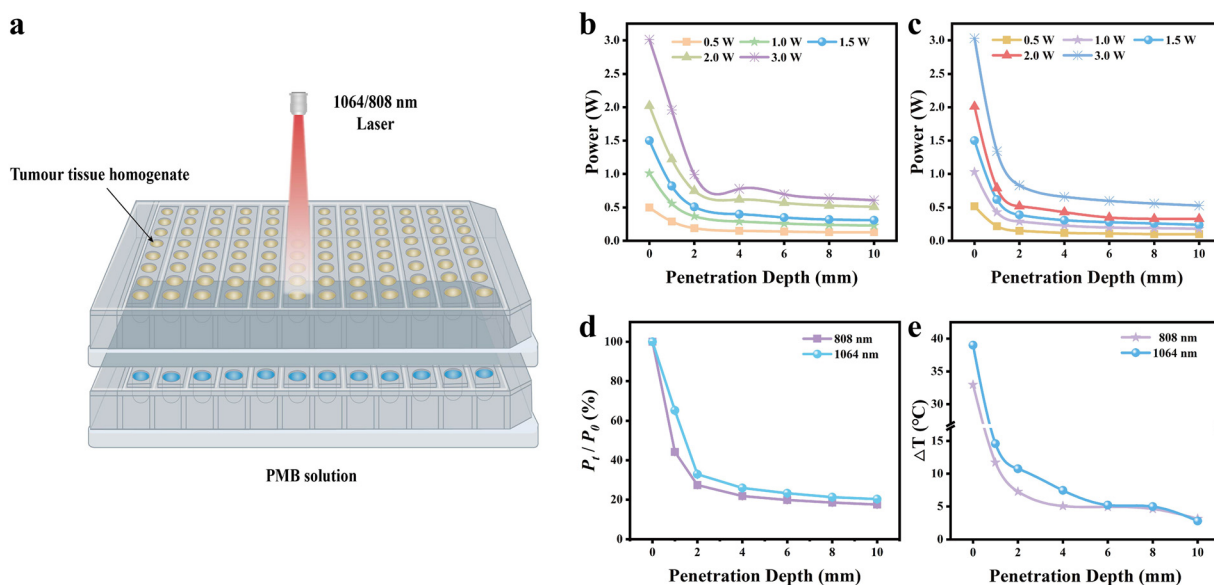

Fig. 3 (a) Schematic diagram of simulated deep tumor environment covered by tumor tissue homogenate above the 96-well plate. The power attenuation of 1064 nm (b) and 808 nm (c) laser under the coverage of tumor homogenates of different thicknesses. (d) Transmitted power density rate of 1064 and 808 nm lasers at different depths tumor tissue homogenate (initial laser power is 3 W). (e) The temperature change of PMB (140.6 μg mL^{-1} 200 μL) at different depths of tumor tissue homogenate under different laser conditions.

and 808 nm lasers after passing through a 1 mm tumor tissue homogenate was measured as 1.96 W and 1.34 W, respectively, and the power attenuation rates of 34.67% and 55.33%.

To further validate the superior tissue penetration and photothermal performance of the 1064 nm laser in deep tissues, we irradiated PMB dispersions covered by tumor tissue homogenates of different thicknesses with 1064 nm and 808 nm laser (3.0 W) for 5 min, respectively (Fig. S9, ESI†). Under identical laser power densities, the temperature rise observed in the PMB dispersion irradiated by the 1064 nm laser exceeded that induced by the 808 nm laser (Fig. 3(e)). For 1 mm thick tumor homogenate, the temperature of the PMB dispersion increased by 14.6 °C and 11.7 °C, respectively. In contrast, the 2 mm thick homogenate temperature rise was 10.7 °C and 7.3 °C, respectively. These results demonstrate that the 1064 nm laser possesses a deeper tissue penetration depth and a superior photothermal effect than the 808 nm laser when penetrating tumor tissue homogenates of identical thickness. However, it is noteworthy that as the thickness of the overlying tissue exceeded 6 mm, the photothermal effect of both lasers began to diminish significantly (less than 5 °C), indicating that these near-infrared lasers have limitations in effectively inducing the penetration depth of photothermal therapy temperature in tumor tissues.

PTT efficacy and *in vitro* safety of PMB

The relative survival rate of 4T1 cells exhibited a concentration-dependent response to PMB. When exposed to 808 nm and 1064 nm laser irradiation, the survival rate of 4T1 cells declined progressively with increasing PMB concentration. Notably, at a PMB concentration of 50 μg mL^{-1}, the survival rate of 4T1 cells under 808 nm laser irradiation was 45.99%, whereas, under 1064 nm laser irradiation, it significantly dropped to 1.82% (Fig. 4(a)). This observation suggests that, at equivalent PMB concentrations, 1064 nm laser irradiation achieves a more potent cell-killing effect. To further assess the impact of laser power on the photothermal efficacy of PMB, we evaluated the relative survival rate of 4T1 cells at varying laser power levels. At laser powers of 1.0, 1.5, and 2.0 W, the survival rate of 4T1 cells under 808 nm laser irradiation was 1.13, 1.05, and 2.46 times higher, respectively, compared to that under 1064 nm laser irradiation (Fig. 4(b) and (c)). It is evident that the survival rate of 4T1 cells decreased inversely with increasing laser power, and at any given laser power, the survival rate was consistently lower under 1064 nm laser irradiation. We utilized 808 nm and 1064 nm lasers to penetrate 2 mm tumor tissue homogenates to evaluate the photothermal treatment efficacy for deep tumors. As the PMB concentration increased, the relative survival rate of 4T1 cells decreased accordingly. Notably, at the same PMB concentration, the photothermal effect of 1064 nm laser irradiation was superior to that of 808 nm. For instance, at a PMB concentration of 100 μg mL^{-1}, the relative survival rate of 4T1 cells after 808 nm and 1064 nm laser irradiation was 76.64% and 43.35%, respectively (Fig. 4(d)). These results further confirm that under identical power and depth conditions, 1064 nm laser irradiation facilitates more effective ablation of tumor cells when combined with PMB, indicating that PMB is a promising photothermal agent for treating deep-seated tumors in the NIR-II regions.
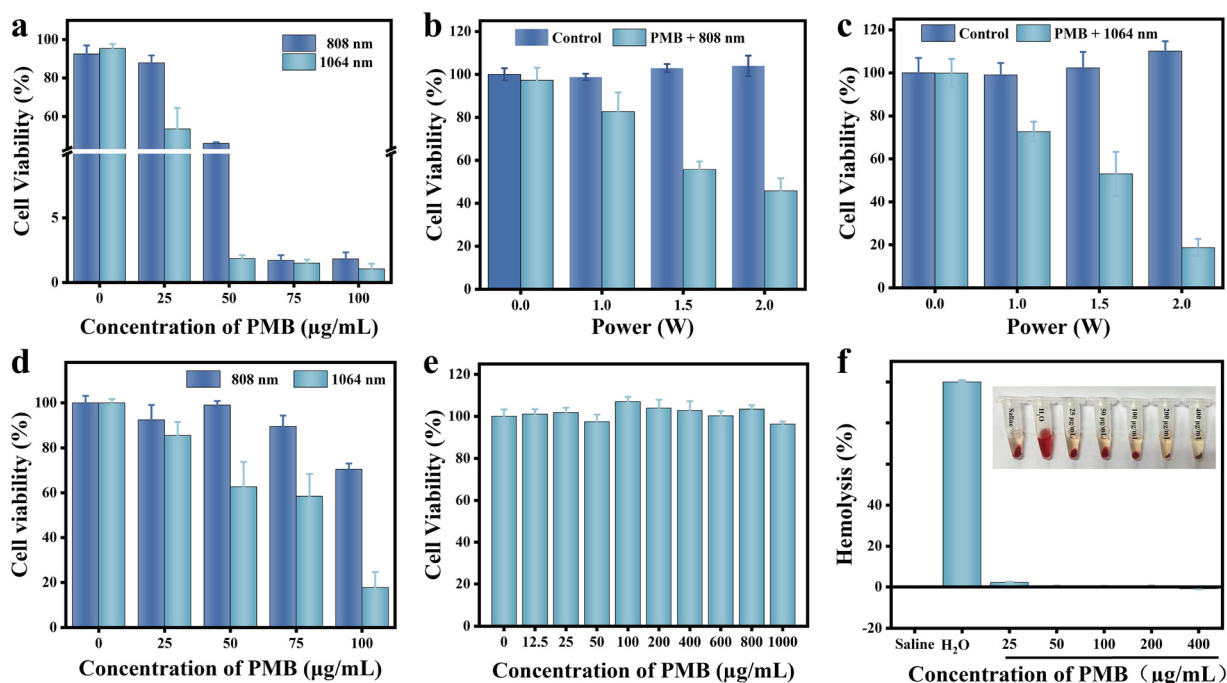

Fig. 4 *In vitro* safety and photothermal properties of PMB. (a) Photothermal effects of different concentrations of PMB under 808 nm and 1064 nm laser irradiation (1 W 5 min). *In vitro* photothermal effect of PMB under different power laser irradiation (b) 808 nm and (c) 1064 nm. (d) Photothermal effects of 808 and 1064 nm laser irradiation of PMB under tumor tissue homogenate (2 mm). (e) Survival rate of 4T1 cells incubated with different concentrations of PMB. (f) Blood compatibility of PMB at various concentrations.

The safety of PMB for cellular use was rigorously assessed using the MTT assay. Remarkably, even at a high concentration of 1000 µg mL^{-1}, the survival rate of 4T1 cells remained at 96.21% (Fig. 4(e)). Furthermore, blood compatibility analysis demonstrated that even with a PMB concentration of 400 µg mL^{-1}, the hemolysis rate was minimal, at only 1.16% (Fig. 4(f)). This hemolysis rate falls below the threshold of 5% specified in ISO 10993-4:2017, indicating no significant

hemolysis occurred. These results convincingly demonstrate that PMB possesses excellent biocompatibility, giving it broad prospects for transformation and applications in the biomedical fields.

The photothermal effect of PMB *in vivo*

The impact of PMB on tumor-bearing mice was examined under 808 nm and 1064 nm laser irradiation. A breast cancer
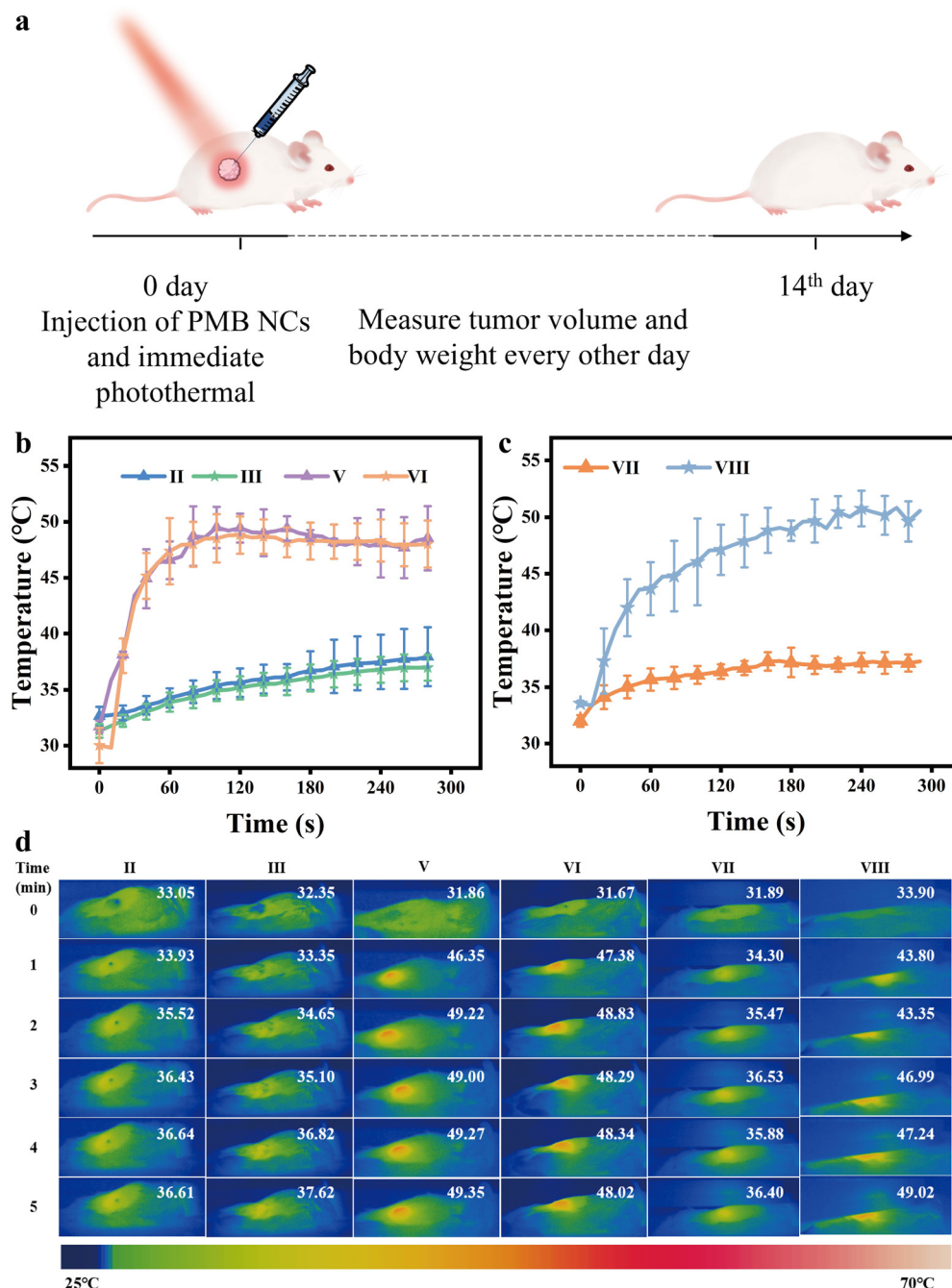

Fig. 5 Evaluation of the efficacy of photothermal treatment of PMB *in vivo* (a) schematic diagram of intratumoral administration of PMB; (b) the temperature rise of tumor region of tumor–bearing mice in different treatment groups (*P* = 1 W, PMB 1.5 mg mL^{-1} 50 µL); (c) temperature maps of mouse tumor sites after 808 nm and 1064 nm laser penetrates 2 mm tumor tissue homogenate; (d) thermogram of tumor area in mice treated under different conditions. (II: saline + 808 nm; III: saline + 1064 nm; V: PMB + 808 nm; VI: PMB + 1064 nm; VII: PMB + 808 nm + cover; VIII: PMB + 1064 nm + cover;).

model was established in Balb/c mice through inoculation with 4T1 tumor cells (Fig. 5(a)). Fig. 5(b) shows the rise in temperature curves of the tumor surface during PTT. Specifically, following intratumoral injection of PMB and irradiation with either 808 nm or 1064 nm laser for 1 minute, the tumor surface temperature promptly rose to 46.6 °C and 47.4 °C, respectively. In contrast, the tumor surface temperature of mice without PMB injection only reached 34.3 °C and 33.9 °C. Notably, the tumor surface temperature of mice treated with PMB remained above 48 °C for 4 minutes of therapy, suggesting that PMB significantly elevates local tumor temperature under 808 nm and 1064 nm laser irradiation.

To validate the superiority of the 1064 nm laser over the 808 nm laser in inducing PTT in deep tissue *in vivo*, PMB was injected into mouse tumor tissue and laser irradiated through a 2 mm layer of tumor tissue homogenate to mimic PTT in deeper tumor regions. As seen in Fig. 5(c), after 5 minutes of irradiation with a 1064 nm laser through the 2 mm tumor homogenate, the tumor surface temperature rapidly increased to 50.6 °C. In contrast, irradiation with an 808 nm laser resulted in a temperature of 36.4 °C in 5 minutes, which did not reach the temperature threshold for tumor ablation (42 °C). The temperature rise experiment results confirm that 1064 nm laser irradiation exhibits a superior heating effect on deep tissue
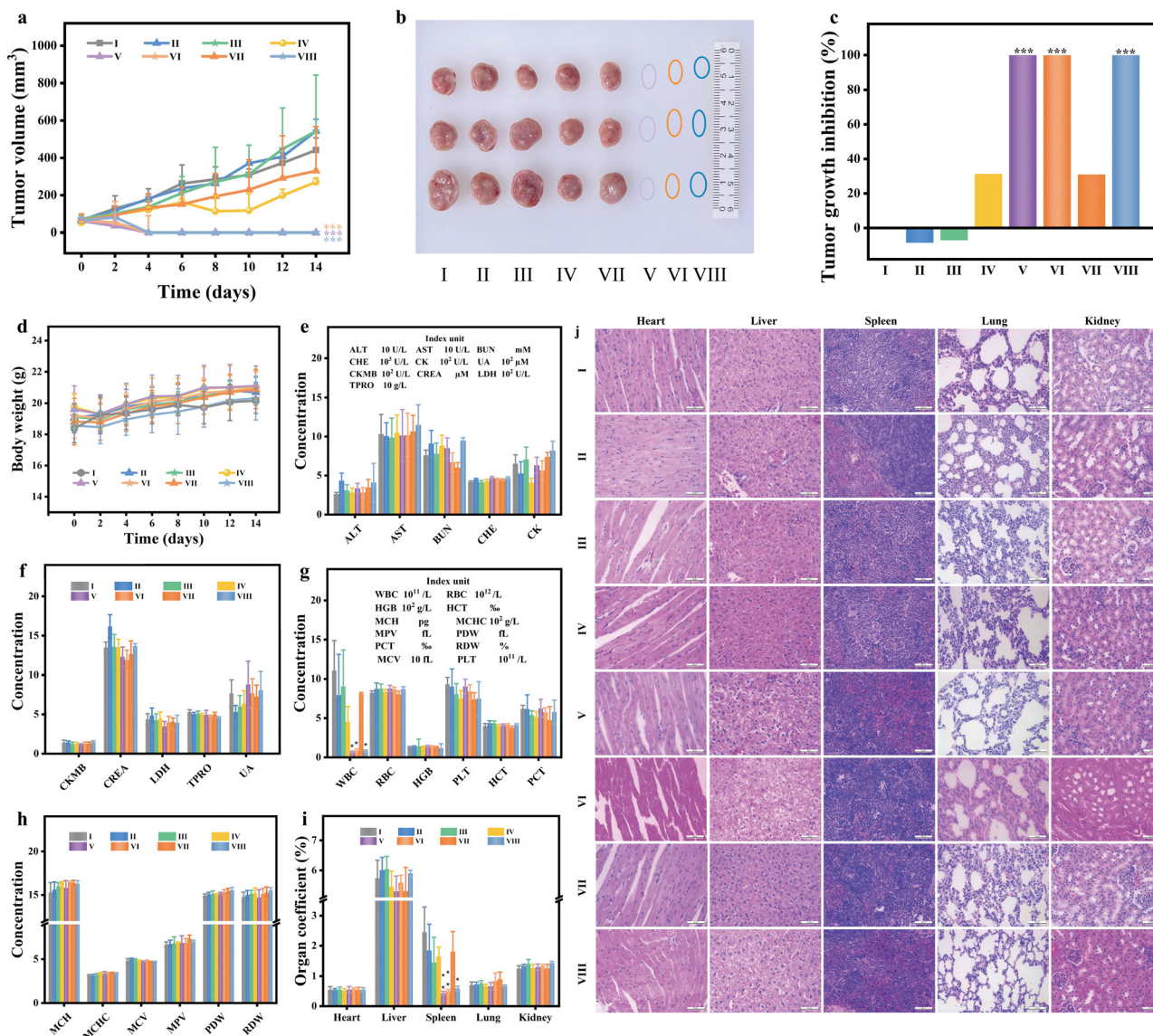

Fig. 6 (a) Quantitative measurement of tumor volume (b) photo of tumor (c) tumor inhibition rate after different treatments. (d) Body weight (e)–(h) blood routine test and serum biochemical indices (i) major organ (heart, liver, spleen, lung, and kidney) coefficient (%) (j) H&E staining of major organs of mice after different treatments for 14 d. n = 3. Data are presented as mean values ± S.D. n.s.: not significant. $p > 0.05$; *$p < 0.05$; **$p < 0.01$; ***$p < 0.001$, analyzed by Student's two-sided test. (I: saline; II: saline + 808 nm; III: saline + 1064 nm; IV: PMB; V: PMB + 808 nm; VI: PMB + 1064 nm; VII: PMB + 808 nm + cover; VIII: PMB + 1064 nm + cover).

compared to 808 nm laser, consistent with our *in vitro* results. Thermal infrared imaging (Fig. 5(d)) further demonstrates the variations in tumor surface temperature in mice after photothermal treatments induced by different NIR lasers.

The *in vivo* photothermal efficacy was evaluated by tracking the relative tumor volumes of treated mice. As illustrated in Fig. 6(a), the tumor growth curves following PTT demonstrate distinct patterns. The tumor growth trends in mice treated with saline, saline + 808 nm, saline + 1064 nm, PMB, and PMB + cover + 808 nm were comparable. By the 14th day, the tumor volumes were 6.71, 7.84, 7.44, 5.10, and 5.02 times the pretreatment tumor volume. In contrast, tumors in the PMB + 808 nm, PMB + 1064 nm laser group, and PMB + cover + 1064 nm group were wholly ablated, and no recurrence signs were observed within 14 days (Fig. 6(b)). Photographs of mice before and after different treatment strategies (Fig. S10, ESI†) visually represent tumor growth in each group, aligning with the tumor growth curve data.

In contrast, the tumor volumes in the other four groups showed no significant differences. The tumor inhibition rates on the final day (Fig. 6(c)) reveal that, compared to the control group, the tumor inhibition rates of the PMB + 808 nm and PMB + 1064 nm groups reached 100%. Notably, in deep tumor tissue, the tumor inhibition rate of the PMB + cover + 1064 nm group also achieved 100%, while the PMB + cover + 808 nm laser irradiation group only exhibited a tumor inhibition rate of 30.98%. Over the 14-day treatment period, the weight of mice in each group showed a gradual upward trend (Fig. 6(d)), with no significant differences observed between groups. The blood biochemical analysis results in Fig. 6(e) and (f) demonstrate no statistical differences between the experimental and control groups following PTT, indicating a favorable safety profile.

Tumor tissue necrosis and decomposition can stimulate the release of myeloid granulocytes, promote the production of granulocytopenia factors by specific tumor cells, and disrupt the regulation of myeloid granulocyte release from the bone
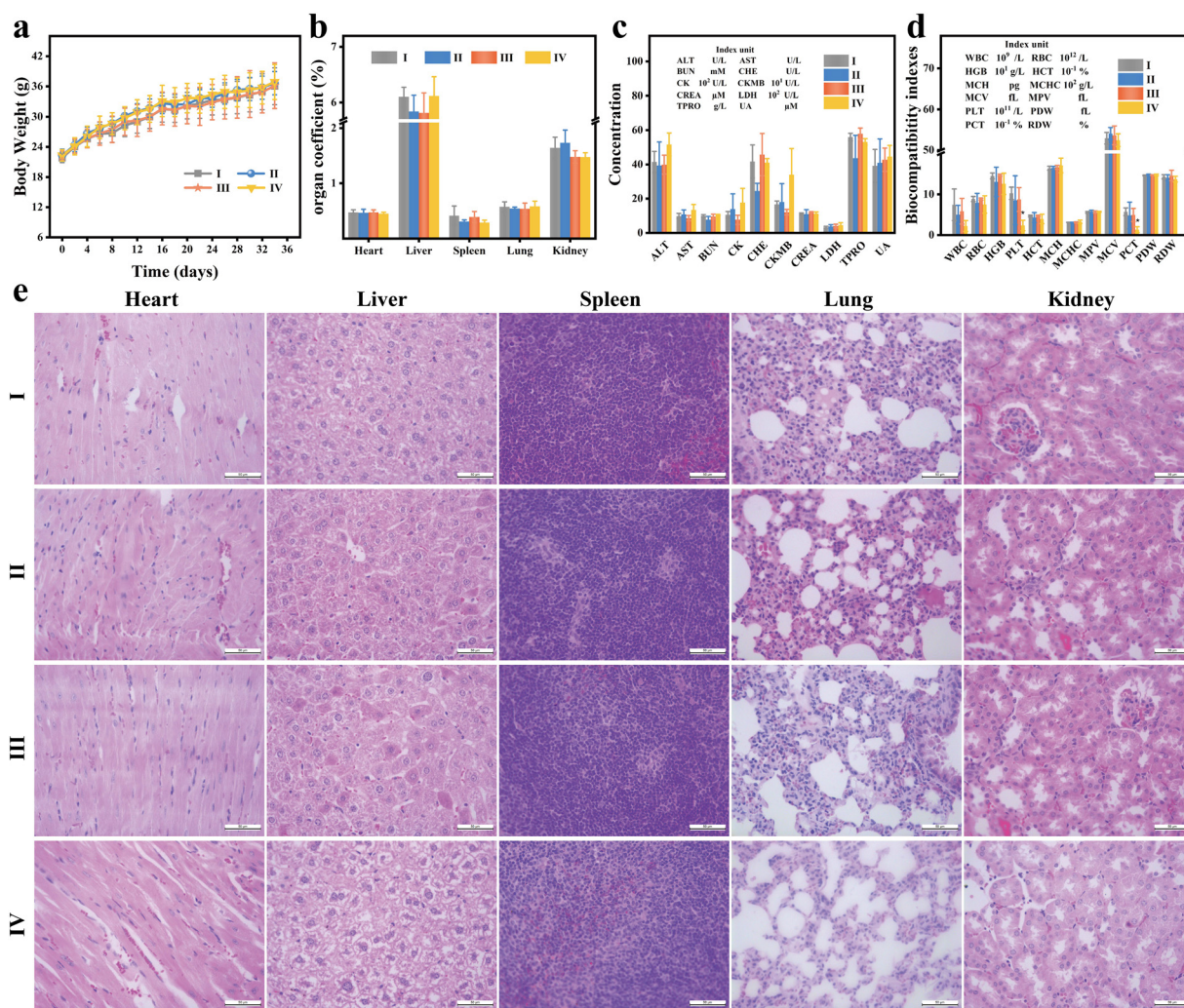

Fig. 7 *In vivo* safety of PMB. (a) Body weight changes of ICR mouse after different concentrations of PMB were injected through the tail vein; (b) major organs (heart, liver, spleen, lungs, and kidneys) coefficient (c) and (d) blood biochemical analysis and (e) H&E-stained images of ICR mice were performed 35 days after caudal intravenous injection of PMB (0, 10, 25, 50 mg kg^{-1}, 100 μL). Data are expressed as mean ± S.D. (n = 5). (I: saline; II: 10 mg kg^{-1} PMB; III: 25 mg kg^{-1} PMB; IV: 50 mg kg^{-1} PMB).

marrow. Additionally, abnormal bodily responses to tumor tissues can lead to leukemoid reactions characterized by elevated white blood cell counts. These leukemoid reactions can also contribute to invasive splenomegaly. However, in the tumor-bearing mice groups (saline, saline + 808 nm, saline + 1064 nm, PMB, PMB + cover + 808 nm), the white blood cell counts were significantly elevated, they were recorded as 110.33 ± 38.39, 79.42 ± 51.51, 90.4 ± 46.40, 45.32 ± 19.49 and $81.53 \pm 1.40 \times 10^9 \text{ L}^{-1}$ (Fig. 6(g) and (h)). This increase is likely due to the leukemoid reaction triggered by the tumor and its necrotic decomposition products. In the tumor-ablation mice groups (PMB + 808 nm, PMB + 1064 nm, and PMB + cover + 1064 nm), the white blood cell counts were notably lower at 6.7 ± 1.42, 8.82 ± 2.05 and $8.17 \pm 1.25 \times 10^9 \text{ L}^{-1}$ respectively. As depicted in Fig. 6(i) and Fig. S11 (ESI†), the organ coefficients revealed that the spleens of mice in the tumor-bearing mice groups were significantly enlarged compared to those in the tumor-ablation mice groups. However, the coefficients of other major organs (heart, liver, lung, kidney) remained unchanged, similar to the control group, suggesting that PMB did not exhibit significant acute toxicity *in vivo*. To further elucidate the impact of PMB on the overall health of the mice, histological analyses using H&E staining showed that the major organs (heart, liver, spleen, lung, and kidney) in all groups exhibited normal structural integrity, resembling the control group. These results indicated no significant pathological abnormalities, such as necrotizing inflammation, were observed within 14 days of treatment (Fig. 6(j)). These findings confirm that PMB, under 808 nm and 1064 nm laser irradiation, possesses a promising photothermal therapeutic effect on tumor-bearing mice, enabling effective thermal ablation of deep tumors, particularly under 1064 nm laser exposure.

In vivo biosafety of PMB

To assess the *in vivo* biosafety of PMB, ICR mice were administered with Saline and varying concentrations of PMB. Over a 35-day observation period, mice exposed to different doses of PMB exhibited normal behavior and survival rates comparable to the control group. The drug-exposed and control groups displayed a consistent upward trend in body weight (Fig. 7(a)), indicating no significant intergroup differences. On day 35, mice were sacrificed, and blood and critical organs (heart, liver, spleen, lungs, and kidneys) were harvested. No noteworthy disparities in organ coefficients were observed among the groups (Fig. 7(b) and Fig. S12, ESI†). Standard blood biochemical markers, including alanine aminotransferase (ALT), aspartate aminotransferase (AST), total protein (TP), globulin (GLB), total bilirubin (TBIL), blood urea nitrogen (BUN), creatinine (CREA), and albumin (ALB), were no significant difference between the PMB-treated and control groups (Fig. 7(c)). It is worth noting that even at a high concentration of 50 mg kg^{-1}, key biochemical indicators of liver and kidney function, such as ALT, AST, and CREA, did not show any abnormalities. The experimental results indicate that PMB concentrations below 50 mg kg^{-1} do not induce hepatotoxicity and nephrotoxicity in mice.

However, excessive molybdenum intake can disrupt the body's metabolism of copper and iron, hinder immune organ development, and compromise immune function, potentially leading to leukopenia.[34,35] Mice treated with a high concentration of PMB (50 mg kg^{-1}) exhibited a slight, though not significant, reduction in white blood cell (WBC) count compared to the control group (Fig. 7(d)). Additionally, platelet (PLT) and blood calcitonin (PCT) levels were significantly reduced, suggesting excessive PMB administration may confer some hematological toxicity. The remaining blood parameters, such as erythrocyte count (RBC), hemoglobin concentration (HGB), hematocrit (HCT), mean erythrocyte hemoglobin (MCH), mean erythrocyte hemoglobin concentration (MCHC), and mean erythrocyte volume (MCV) did not differ significantly between the high-concentration PMB group and the control group. Further, histological analysis through H&E staining of major organs (Fig. 7(e)) revealed no notable histological differences or injuries in the tissue sections of the PMB-treated mice. These findings strengthen the evidence that low doses of PMB exhibit no acute toxicity *in vivo* for mice and possess excellent biocompatibility.

Conclusions

In this study, we harnessed the phosphoric acid of ssDNA to react with ammonium molybdate, resulting in a novel photothermal preparation designated as PMB. PMB exhibits robust absorption in both NIR-I and NIR-II regions, boasting high photothermal conversion efficiency, excellent thermal stability, favorable biocompatibility, and a sensitive pH response. Our *in vitro* experiments on breast cancer cells and tumor-bearing mice revealed that PMB exerts a significant photothermal ablation effect in NIR-I and NIR-II regions, with no discernible side effects. Notably, under 1064 nm laser irradiation, PMB achieves deeper tumor penetration compared to 808 nm excitation, indicating its potential for treating deeper tumors. Consequently, PMB holds promising prospects as a unique photothermal agent for deep tumor therapy, and this research offers a compelling strategy for developing nano-photothermal agents with strong NIR-II absorption and deep tissue penetration.

Materials and methods

Materials

DNA was synthesized and purified by Shanghai Sangon Biotechnology Co., LTD with the sequence (5′ to 3′) being ATCGTC-GATGCTAATCCTGA. The hydrochloric acid (HCl, ~36%) was sourced from Sinopharm Group. The 4% paraformaldehyde fixative was procured from Beyotime Biotechnology Co., LTD (Shanghai, China). Ascorbic acid, ammonium molybdate tetrahydrate (99.9%) ($H_{24}Mo_7N_6O_{24} \cdot 4H_2O$), and thiazolium blue tetrazolium bromide (98%) (3-(4,5-dimethylthiazol-2-yl)-2,5-diphenyl tetrazolium bromide, MTT) were obtained from Aladdin (Shanghai, China). The RPMI 1640 culture medium, fetal

bovine serum (FBS), penicillin–streptomycin L-glutamine, and trypsin-EDTA (0.25%) were purchased from Gibco Laboratories (Grand Island, NY, USA). The 4T1 murine mammary cancer cell line was acquired from Shanghai Cell Bank, Chinese Academy of Sciences. Additionally, Balb/c mice (Certificate number: 20230706Abzz0100999613) and ICR mice (Certificate number: 20230621Azbb0100999819) were purchased from Hangzhou Qizhen Laboratory Animal Technology Co., LTD (Hangzhou, China), with the production license number being SCXK (Zhe) 2022-0005.

All chemicals were used without further purification. Unless otherwise specified, all experiments were carried out at room temperature. Furthermore, all animal experiments were conducted using protocols approved by the Animal Ethics Research Committee at Shaoxing People's Hospital (license no. SYXK (Zhe) 2017-0007).

Equipments

The morphology of PMB nanoparticles was characterized using transmission electron microscopy (TEM, JEM-1011, Japan). The dynamic light scattering (DLS) and zeta potential were measured *via* a Malvern Panalytical Zetasizer Nano ZS90 size analyzer. An energy spectrum component was coupled with a high-resolution transmission electron microscope (HRTEM, JEOL JEM-2100F, Japan) to determine the composition and distribution of elements in PMB. The UV-visible-near-infrared spectrometer (UV-3600 Plus, Shimadzu, Japan) was used to analyze the visible-near-infrared absorption spectrum. Fourier transform infrared (FTIR) spectroscopy was performed on the Nicolet Nexus 870 spectrometer (Thermo Scientific, USA). A thermal imager (PI400, Optris, Germany) recorded real-time sample temperature and thermal images. Laser power was measured with a digital power meter (DP-LPE-1B, Beijing, Eurasia, Germany). Lastly, Spectra Max i3 (Molecular Devices, USA) was utilized to determine the absorbance values of the samples at specific wavelengths.

Experimental method

Preparation of PMB Nanoparticles

A straightforward one-step hydrothermal synthesis self-assembly technique synthesized PMB nanoparticles. Initially, 60 μL of 10% HCl aqueous solution is added to 1000 μL of 2% $(NH_4)_2MoO_4$ aqueous solution and vortexed for 5 s. Subsequently, 100 μL of 25 μM ssDNA aqueous solution was added, thoroughly vortexed, and followed by the addition of 1000 μL of 10% VC aqueous solution. As the reaction proceeds, the color of the reaction solution changes from colorless to the initial yellow and gradually changes to dark blue with temperature increasing. The reaction mixture was then incubated in a water bath at 95 °C for 6 hours, forming dark blue PMB nanoparticles. The obtained nanoparticles were then transferred into a 3000 Da ultrafiltration tube and centrifuged at 5000 rpm for 30 minutes. Finally, the purified PMB nanoparticles are redispersed in deionized water and stored in a refrigerator at −20 °C for further use.

PMB photothermal performance evaluation

The temperature rise curve was determined by placing 1 mL of PMB dispersions, each with varying concentrations ranging from 0 to 234.3 μg mL^{-1} (0, 46.8, 93.7, 140.6, 187.4, and 234.3 μg mL^{-1}), in a quartz cell. These dispersions were then irradiated with NIR lasers of 808 nm and 1064 nm wavelengths, respectively, at a power of 2.0 W for 5 minutes at room temperature. The thermal imager captured the temperature changes of the PMB dispersions, taking a thermal image every minute.

Subsequently, using the same methodology, PMB dispersions with a fixed concentration of 140.6 μg mL^{-1} were irradiated with 808 nm and 1064 nm lasers, each operating at different powers spanning from 0 to 2.5 W (0, 0.5, 1.0, 1.5, 2.0, and 2.5 W). The dispersions were exposed for 5 minutes, and the temperature and corresponding thermal images of the PMB dispersions were recorded.

For the photothermal repeatability curve analysis, a PMB dispersion with a concentration of 140.6 μg mL^{-1} was irradiated for 5 minutes using NIR lasers with wavelengths of 808 nm and 1064 nm, both operating at a power of 2.0 W. After each irradiation cycle, the laser was switched off, allowing the PMB dispersion cooling for 5 minutes. This heating–cooling cycle was repeated five times. The temperature of the PMB dispersion was monitored in real time, and the resulting repeatability curve depicting the rise and fall of temperatures was plotted accordingly.

For the analysis of the rising and cooling curves, a PMB dispersion solution with a concentration of 140.6 μg mL^{-1} was irradiated using NIR lasers with wavelengths of 808 nm and 1064 nm, both operating at a power of 2.0 W. Once the PMB dispersion reached thermal equilibrium, the lasers were switched off, allowing the dispersion to cool down to room temperature naturally. The temperature of the PMB dispersion was recorded continuously, and the rising and cooling curves were subsequently plotted. The photothermal conversion efficiency (η) of PMB under both 808 nm and 1064 nm laser irradiation was calculated, referring to the methodology outlined by Geng.[36]

Tissue penetration depth determination by 808 nm and 1064 nm laser

After the 808 nm and 1064 nm lasers penetrated tumor tissue homogenates of varying thicknesses (0, 2, 4, 6, 8, and 10 mm) at different powers (0.5, 1.0, 1.5, 2.0, and 3.0 W), the residual laser power after penetrating each layer was accurately measured using a digital power meter. Subsequently, 200 μL of PMB dispersion solution (140.6 μg mL^{-1}) was placed in a 0.2 mL EP tube, which was then topped with tumor tissue homogenates of varying thicknesses (0, 2, 4, 6, 8, and 10 mm). These samples were irradiated with 808 nm and 1064 nm lasers (3.0 W) for 5 minutes each. The infrared thermal imager recorded the temperature of the PMB dispersion every 10 s,

enabling the plotting of a laser power attenuation curve that reflects the penetration efficiency through the tumor tissue homogenates.

Cell culture *in vitro*

Mouse triple-negative breast cancer cells (4T1) were cultivated in a standardized environment using RPMI-1640 medium supplemented with 10% heat-inactivated fetal bovine serum (FBS) and 1% penicillin–streptomycin. These cells were incubated in a humified incubator (37 °C, 5% CO_2).

Evaluation of cytotoxicity of PMB *in vitro*

The *in vitro* cytotoxicity of PMB was evaluated through a standard methylthiazole tetrazolium (MTT) assay. Logarithmically growing 4T1 cells were seeded in 96-well plates at a density of 10^4 cells per well, and 100 μL of RPMI-1640 medium was added to each well. The original medium was discarded after overnight incubation, and the cells were washed with PBS. Subsequently, 100 μL of medium containing varying concentrations of PMB (0, 100, 200, 400, 600, 800, and 1000 μg mL^{-1}) was added to each well, with six replicate wells per concentration group. The cells were further incubated for 24 hours. After incubation, the PMB-containing medium was discarded, and the cells were washed with PBS. Then, 100 μL of 1640 medium and 10 μL of MTT (5 mg mL^{-1}) were added to each well. The cells were incubated for 4 hours, and subsequently, the supernatant was carefully aspirated. Following this, 150 μL of DMSO was added to each well. The 96-well plate was then placed in a microplate reader and shaken for 10 minutes, and the absorbance values at 490 nm were recorded for each well. The relative cell survival rate was calculated using the formula $CV = A/A_0 \times 100$, where CV represents the cell survival rate, A is the absorbance value at 490 nm of the PMB-treated group, and A_0 is the absorbance value at 490 nm of the blank control group.

The orbital blood was collected from healthy Balb/c mice and put into anticoagulant tubes to assess the potential hemolytic properties of PMB. A volume of 160 μL of whole blood was extracted and blended with 2 mL of saline solution. The mixture was centrifuged at 300 rpm for 5 minutes, and the supernatant was carefully discarded. Then, an additional 2 mL of saline solution was added, and the centrifugation was repeated twice to achieve a clear supernatant. Ultimately, the red blood cells were resuspended in 2 mL of Saline, representing a volume concentration of 8% (v_0/v). Multiple 1.5 mL EP tubes were prepared, each containing 400 μL of Saline (experimental group), deionized water (positive control), or Saline (negative control) with varying concentrations of PMB (0, 25, 50, 100, 200, and 400 μg mL^{-1}). 400 μL of the red blood cell suspension was added. The EP tubes were incubated in a 37 °C water bath for 30 minutes. After incubation, the EP tubes were taken out of the water bath and centrifuged at 300 rpm for 5 minutes. The extent of hemolysis was visually observed and photographed. Subsequently, 200 μL of the supernatant from each tube was carefully transferred to a 96-well plate and analyzed in a microplate reader to measure the optical density (OD) at 545 nm. The hemolysis rate was calculated using the formula: hemolysis rate = $(OD_{experimental} - OD_{negative})/(OD_{positive} - OD_{negative}) \times 100\%$.

PMB photothermal experiment *in vitro*

The 4T1 cells were seeded into 96-well plates at 10^4 cells per well and supplemented with 100 μL of 1640 medium to evaluate the PTT efficacy of PMB on tumor cells. The plates were incubated overnight in a suitable environment. The original medium was discarded the following day, and the wells were gently washed with Saline. Subsequently, 100 μL of Saline containing varying concentrations of PMB (0, 25, 50, 75, and 100 μg mL^{-1}) was added to each well, with four replicate wells per concentration group. Immediately, each well was irradiated with either an 808 nm or 1064 nm laser at 1.0 W for 5 minutes. Post-irradiation, the cells were washed with PBS, replenished with 100 μL of 1640 medium, and cultured for 24 hours. After this period, the cell viability was assessed using an MTT assay. The 4T1 cells were irradiated with 808 nm and 1064 nm lasers at different power densities (0, 0.5, 1.0, and 2.0 W cm^{-2}) using the same culturing protocol to determine the optimal PTT conditions. The cell survival rates under various PTT conditions were then measured.

Evaluation of the photothermal effect of PMB *in vitro* under deep tissue

The 4T1 cells were seeded into 96-well plates at 10^4 cells per well and supplemented with 100 μL of 1640 medium. The plates were incubated overnight in a suitable environment, and then the original medium was carefully removed, and the wells were washed with Saline. Subsequently, 100 μL of Saline containing varying concentrations of PMB (0, 25, 50, 75, and 100 μg mL^{-1}) was added to each well, with four replicate wells per concentration group. Immediately, the wells were irradiated for 5 minutes with 808 nm or 1064 nm lasers (3.0 W) through tumor tissue homogenate with 2 mm thickness. After irradiation, the cells were washed with PBS, replenished with 100 μL of 1640 medium, and cultured for 24 hours. Finally, the cell viability was assessed using an MTT assay.

Evaluation of efficacy of photothermal therapy for PMB *in vivo*

50 μL of a suspension containing 10^6 4T1 cells was inoculated into the subcutaneous region of the right lower back of female Balb/c mice aged 5–6 weeks. Once the tumor reached a volume of 50–60 mm^3, the mice were randomly allocated to six groups: I, II, III, IV, V, and VI. The groups received the following treatments: I: saline (50 μL); II: saline (50 μL) + 808 nm laser; III: saline (50 μL) + 1064 nm laser; IV: PMB (50 μL, 1.5 mg mL^{-1}); V: PMB (50 μL, 1.5 mg mL^{-1}) + 808 nm laser, and VI: PMB (50 μL, 1.5 mg mL^{-1}) + 1064 nm laser. The laser power was set at 1.0 W in the laser-irradiated groups, and the irradiation duration was 5 minutes. After treatment under various conditions, the tumor volume was measured using a vernier caliper every other day, and the body weight of the mice was recorded. The tumor volume was calculated using the formula $V = L \times W^2/2$, where V represents the tumor volume, L is the length, and W is the width. After two weeks of treatment, the

mice were euthanized, and orbital blood collection was performed to routine the blood and serum biochemical analysis. Additionally, H&E staining was conducted on major organs (heart, liver, spleen, lung, and kidney) to assess potential toxicity or histological changes.

Evaluation of photothermal efficacy in deep tumor

A subcutaneous injection of 50 μL containing 10^6 4T1 cells was administered on the lower right side of the back of Balb/c mice. Once the tumor reached a volume of 50–60 mm^3, the mice were randomly divided into two groups: VII and VIII. Group VII received PMB (50 μL, 1.5 mg mL^{-1}) combined with a cover and irradiation using an 808 nm laser. In comparison, Group VIII received PMB (50 μL, 1.5 mg mL^{-1}) combined with a cover and irradiation using a 1064 nm laser. In both groups, the "cover" refers to a 2 mm layer of tumor tissue homogenate placed over the mouse tumor. This layer allowed the 808 nm and 1064 nm lasers to penetrate through the tissue homogenate and irradiate the tumor site. The laser power was set at 3.0 W, and irradiation was performed for 5 minutes. The evaluation methods for tumor efficacy are consistent with the above experiments.

Evaluation of *in vivo* toxicity of PMB

After one week of adaptive feeding, twenty male ICR mice (aged 4–5 weeks, 20 g) were randomly assigned to four groups of five mice each. These mice were injected with 100 μL of Saline, 10 mg kg^{-1} PMB, 25 mg kg^{-1} PMB, and 50 mg kg^{-1} PMB dispersions *via* the tail vein. The following day, the mice were weighed, and their growth, eating, and mental state were observed. After 35 days of feeding, the mice were euthanized, and blood samples were collected *via* orbital puncture for routine blood and serum biochemical analysis. H&E staining and histological examinations were performed on the main organs to determine potential toxicity or histological changes.

Statistic analysis

The experimental data were analyzed using Origin 2021 statistical software. All values are presented as mean ± standard deviation (S.D.). A single-factor analysis of variance (ANOVA) was used to compare the experimental data across various groups, and a *T*-test was further utilized for pairwise comparisons. Statistical significance was set at $p < 0.05$, denoted by (*) for $p < 0.05$ and (**) for $p < 0.01$.

Author contributions

Baoru Fang: investigation, methodology, visualization, writing – original draft. Siqi Geng: formal analysis, methodology. Ke Wang: data curation, investigation. Fang Wang: investigation. Yiqing Zhou: data curation. Jiaying Qin: formal analysis. Shengnan Luo: data curation. Yanping Chen: methodology, visualization. Zhangsen Yu: conceptualization, supervision, funding acquisition, project administration, writing – review & editing.

Data availability

All the data that support this study are included in this article and its ESI.†

Conflicts of interest

There are no conflicts to declare.

Acknowledgements

Notes and references

1 Y. Chen, Y. Wu, B. Sun, S. Liu and H. Liu, *Small*, 2017, **13**(10), 1603446.
2 Y. Wang, W. Du, T. Zhang, Y. Zhu, Y. Ni, C. Wang, F. M. Sierra Raya, L. Zou, L. Wang and G. Liang, *ACS Nano*, 2020, **14**(8), 9585–9593.
3 X. Li, J. F. Lovell, J. Yoon and X. Chen, *Nat. Rev. Clin. Oncol.*, 2020, **17**(11), 657–674.
4 H. Liu, C. Gao, P. Xu, Y. Li, X. Yan, X. Guo, C. Wen and X. C. Shen, *Small*, 2024, **20**(42), e2401117.
5 H. Lin, S. Gao, C. Dai, Y. Chen and J. Shi, *J. Am. Chem. Soc.*, 2017, **139**(45), 16235–16247.
6 X. Wu, Y. Suo, H. Shi, R. Liu, F. Wu, T. Wang, L. Ma, H. Liu and Z. Cheng, *Nano-Micro Lett.*, 2020, **12**(1), 38.
7 B. Chang, D. Li, Y. Ren, C. Qu, X. Shi, R. Liu, H. Liu, J. Tian, Z. Hu, T. Sun and Z. Cheng, *Nat. Biomed. Eng.*, 2022, **6**(5), 629–639.
8 B. Guo, Z. Sheng, D. Hu, C. Liu, H. Zheng and B. Liu, *Adv. Mater.*, 2018, **30**(35), e1802591.
9 Q. Zhu, W. Jiang, K. Ye, S. Jin, W. Dong, S. Liu, G. Zhang, C. Tian, Y. Luo, Y. Wang and J. Jiang, *Adv. Funct. Mater.*, 2021, **32**, 1–39.
10 H. Xiang, L. Zhao, L. Yu, H. Chen, C. Wei, Y. Chen and Y. Zhao, *Nat. Commun.*, 2021, **12**(1), 218.
11 W. Yin, T. Bao, X. Zhang, Q. Gao, J. Yu, X. Dong, L. Yan, Z. Gu and Y. Zhao, *Nanoscale*, 2018, **10**(3), 1517–1531.
12 Y. Han, B. Qu, J. Li, X. Zhang, X. Peng, W. Li and R. Zhang, *J. Inorg. Biochem.*, 2020, **209**, 111121.
13 Y. Zhu, R. Zhao, L. Feng, C. Wang, S. Dong, M. V. Zyuzin, A. Timin, N. Hu, B. Liu and P. Yang, *ACS Nano*, 2023, **17**(7), 6833–6848.
14 D. Zhang, J. Zhang, Q. Li, H. Tian, N. Zhang, Z. Li and Y. Luan, *ACS Appl. Mater. Interfaces*, 2018, **10**(36), 30092–30102.

15 C. Y. Zhou, L. Zhang, T. Sun, Y. Zhang, Y. D. Liu, M. F. Gong, Z. S. Xu, M. M. Du, Y. Liu, G. Liu and D. Zhang, *Adv. Mater.*, 2020, **33**(3), 2006532.

16 P. Xu, C. Wen, C. Gao, H. Liu, Y. Li, X. Guo, X. C. Shen and H. Liang, *ACS Nano*, 2024, **18**(1), 713–727.

17 Z. Zhou, J. Xie, S. Ma, X. Luo, J. Liu, S. Wang, Y. Chen, J. Yan and F. Luo, *ACS Omega*, 2021, **6**(16), 10723–10734.

18 S. Sun, J. Chen, K. Jiang, Z. Tang, Y. Wang, Z. Li, C. Liu, A. Wu and H. Lin, *ACS Appl. Mater. Interfaces*, 2019, **11**(6), 5791–5803.

19 C. Murugan, V. Sharma, R. K. Murugan, G. Malaimegu and A. Sundaramurthy, *J. Controlled Release*, 2019, **299**, 1–20.

20 A. Soleimany, S. Khoee, S. Dias and B. Sarmento, *ACS Appl. Mater. Interfaces*, 2023, **15**(17), 20811–20821.

21 X. Huang, W. Zhang, G. Guan, G. Song, R. Zou and J. Hu, *Acc. Chem. Res.*, 2017, **50**(10), 2529–2538.

22 C. V. Krishnan, J. Chen, C. Burger and B. Chu, *J. Phys. Chem. B*, 2006, **110**(41), 20182–20188.

23 Z. Wang, P. K. Upputuri, X. Zhen, R. Zhang, Y. Jiang, X. Ai, Z. Zhang, M. Hu, Z. Meng, Y. Lu, Y. Zheng, K. Pu, M. Pramanik and B. Xing, *Nano Res.*, 2019, **12**(1), 49–55.

24 Y. Y. Wang, W. L. Wang, X. C. Shen, B. Zhou, T. Chen, Z. X. Guo, C. C. Wen, B. P. Jiang and H. Liang, *ACS Appl. Mater. Interfaces*, 2018, **10**(49), 42088–42101.

25 Y. Wang, F. Gong, Z. Han, H. Lei, Y. Zhou, S. Cheng, X. Yang, T. Wang, L. Wang, N. Yang, Z. Liu and L. Cheng, *Angew. Chem., Int. Ed.*, 2023, **62**(9), e202215467.

26 G. Song, J. Shen, F. Jiang, R. Hu, W. Li, L. An, R. Zou, Z. Chen, Z. Qin and J. Hu, *ACS Appl. Mater. Interfaces*, 2014, **6**(6), 3915–3922.

27 D. Ding, W. Guo, C. Guo, J. Sun, N. Zheng, F. Wang, M. Yan and S. Liu, *Nanoscale*, 2017, **9**(5), 2020–2029.

28 H. Zu, Y. Guo, H. Yang, D. Huang, Z. Liu, Y. Liu and C. Hu, *New J. Chem.*, 2018, **42**, 18533–18540.

29 M. Li, C. Wang, Z. Di, H. Li, J. Zhang, W. Xue, M. Zhao, K. Zhang, Y. Zhao and L. Li, *Angew. Chem., Int. Ed.*, 2019, **58**(5), 1350–1354.

30 M. A. Hussein, T. S. Guan, R. A. Haque, M. B. Khadeer Ahamed and A. M. Abdul Majid, *Spectrochim. Acta, Part A*, 2015, **136**, 1335–1348.

31 G. Wang, H. Wang, S. Cao, W. Xiang, T. Li and M. Yang, *Mikrochim. Acta*, 2019, **186**(2), 96.

32 J. Zhao, Z. Li, Y. Shao, W. Hu and L. Li, *Angew. Chem., Int. Ed.*, 2021, **60**(33), 17937–17941.

33 D. Patel, S. Thankachan, P. P. Abu Fawaz, T. Venkatesh, S. Prasada Kabekkodu and P. S. Suresh, *Mitochondrion*, 2023, **70**, 118–130.

34 U. Yadav, V. Singh, H. Mishra, P. S. Saxena and A. Srivastava, *Bio. Rxiv.*, 2021, **5**, 443109.

35 F. J. Liu, W. Y. Dong, H. Zhao, X. H. Shi and Y. L. Zhang, *Theriogenology*, 2019, **126**, 49–54.

36 S. Geng, Q. Feng, C. Wang, Y. Li, J. Qin, M. Hou, J. Zhou, X. Pan, F. Xu, B. Fang, K. Wang and Z. Yu, *J. Nanobiotechnol.*, 2023, **21**(1), 338.